Chapter 3

Engendering Plain and Hierarchical Molybdenum Sulfide Nanostructures via Conventional and Microwave Assisted Hydro/Solvo-Thermal Routes

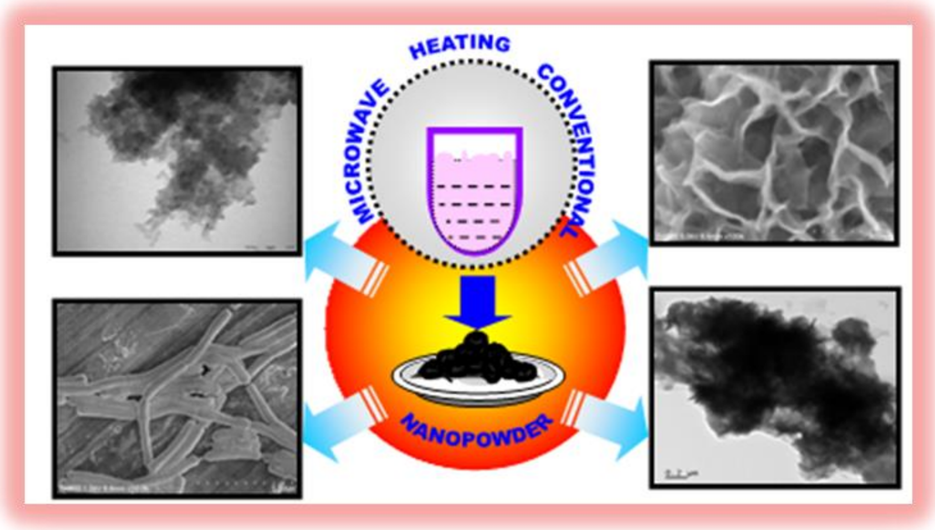

“An experiment is a question which science poses to Nature, and a measurement is the recording of Nature’s answer.”

-MAX PLANCK, (1858 TO 1947)

3.1 Introduction

Molybdenum sulfide is an interesting class of materials exhibiting very interesting properties in its 0D, 1D, 2D and 3D forms [1-5]. Among different molybdenum sulfide compounds, molybdenum disulfide (MoS_2) is the most important and is being researched fundamentally, computationally and experimental all over the world. The properties, synthesis methods, and applications of this wonder material have already been mentioned in chapter 2. It may, however, be noted that synthesis of MoS_2 nanostructures using solvothermal method is reported scarcely [6, 7]. Also, there are no reports pertaining to its synthesis using microwave assisted solvothermal method route. From an application point of view, MoS_2 nanostructures have not been explored in antimicrobial applications at all. Owing to its biocompatible nature [8], it was decided to explore microbial investigations comprehensively which indeed formed the important asset of this chapter.

Therefore, the present chapter deals with the synthesis of plain and hierarchical MoS_2 nanostructures using conventional and microwave assisted hydro/solvothermal route. The chapter can be divided into two main sections. The first section involves the synthesis of hierarchical nanostructures of MoS_2 using conventional hydro/solvothermal method. Owing to their high surface area, such hierarchical nanostructures may be useful for different biological and electronics applications. The second section deals with microwave assisted solvothermal synthesis of MoS_2 nanostructures and their antimicrobial applications. The speculative mechanism of antimicrobial action has also been explained backed by different enzymatic activity studies. Hierarchical nanostructures of MoS_2 are very imported from the standpoint of their applications in different fields as they simultaneously possess bulk nature due to a bigger size as well as quantum confinement effects due to nanosheet-like nature of petals. So far MoS_2 nanoflowers have been reported using different methods such as solvothermal route, sol-gel route, chemical process, etc [9-12].

3.2 Synthesis of Molybdenum Sulfide Nanostructures MSNs via Conventional Hydrothermal Route

3.2.1 Experimental

3.2.1.1 Synthesis of MoS_2 nanoparticles

All chemicals were of reagent grade and were used as received. The synthesis of molybdenum metal was carried out through hydrothermal assisted route. In one beaker, molybdenum precursor (molybdenum chloride) was taken with 30 ml of deionized water (DIW) stirred for 20 minutes till it dissolved. Similarly, in another beaker thiourea was taken in 30 ml of DIW stirred for 20 minutes with molar ratio 1:3. This mixture was stirred for another 20 minutes and poured in stainless steel autoclave and placed in an oven. The sealed 100 mL Teflon lined autoclaves containing above solution mixture were placed for hydrothermal treatment at 200 ^{o}C for 9 and 21 hrs respectively, for two separate reactions. The oven is allowed to cool naturally to room temperature. Subsequently, the resulting black solid was retrieved from the solution by centrifugation, washed with distilled water followed by ethanol two times to remove the ions possibly remaining in the end product, and finally dried at 60 °C for 6 hrs respectively. The experimental procedure is depicted in figure 3.1. The samples prepared corresponding to the reaction time of 9 h, and 21 h are labeled as MS9 and MS21, respectively.

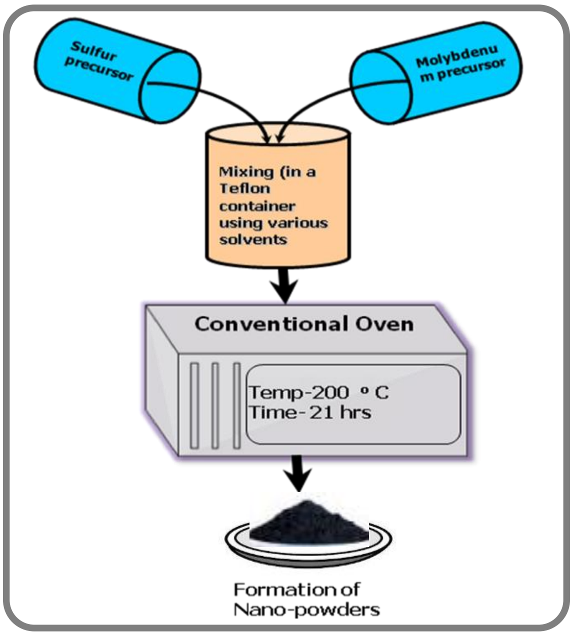

Figure 3.1 *Flow-diagram illustrating the process steps used for synthesis of MoS_2 nanopowders.*

3.2.1.2 Characterization of MoS_2 nanoparticles

The structural information on virgin powder samples was obtained using X-ray diffraction (Bruker D8 Advance) technique. The diffracting angle 2(θ) was varied between 10 - 80° range and the observed XRD peaks were compared with standard JCPDS cards. The surface morphological features of the same were investigated by field emission scanning electron microscopy (FESEM) using HITACHI S-4800. The power sample was directly dropped on the conducting carbon film and was coated with a thin Au-Pd film by sputtering to avoid the effects due to the charging of sample. The microstructure of the samples was investigated by field emission transmission electron microscope (FETEM) with JEM-2200FS (JEOL, Japan), at an acceleration voltage of 200 KV. The samples for FETEM were prepared by dispersing fine powder of the resultant product in isopropyl alcohol. A drop of dispersion was then transferred to carbon coated grid for further analysis.

3.2.2 Results and discussion

3.2.2.1 X-ray diffraction

The X-ray diffractograms for the as-synthesized powder samples are represented in figure 3.2. Both the samples MS9 and MS21 reveal the formation of hexagonal MoS_2 as the predominant phase. However, for MS9 sample (figure 3.2a), $Mo_{15}S_{19}$ has also been found out as the minor phase. The relatively small intensity peaks at 11.04, 12.5, 14.3, 43.04 and 45.4 can be ascribed to $Mo_{15}S_{19}$ (JCPDS card # 40-0936). Two broad humps centered around 2θ ~ 33° and 57° can be correlated with the peaks at 32.89°, 33.4° & 35.3° and 56.2° and 58.3°, respectively, which can be matched well with MoS_2 phase (JCPDS card # 37-1492). It may be noted that the peaks for $Mo_{15}S_{19}$ also exist in the region ~ 33°. Nevertheless, because of the presence of major peaks both at ~ 33° and 57°, it can be inferred that MoS_2 is the dominant phase in this sample. Similar behaviour is also noticed in the case of sample MS21 (figure 3.2b). However, $Mo_{15}S_{19}$ has not been noticed as the minor phase hinting that phase pure MoS_2 is produced when the reaction was carried out for 21h.

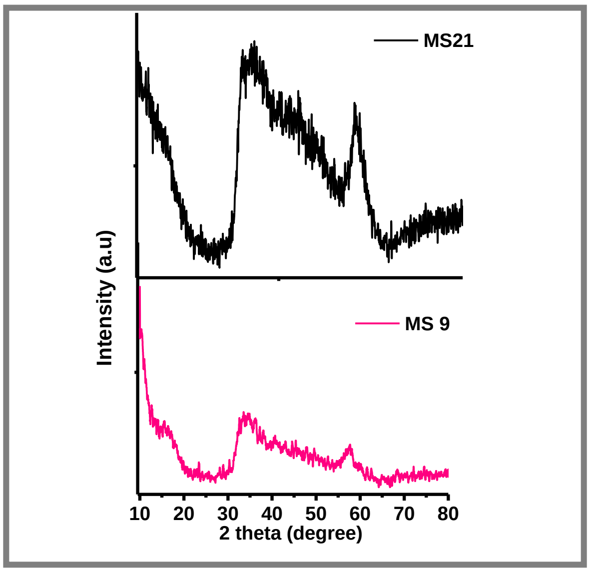

Figure 3.2 *X-ray diffractograms of resultant powder samples, MS9 and MS21.*

Another remarkable feature emanating from the diffractogram is the absence of a peak at 58.3°. Therefore, instead of a broad peak around ~

57°, singlet peak at 56.2° was found out. $Mo_{15}S_{19}$ as a minor phase for the reaction of 9h may arise due to the incomplete reaction which leads to a stoichiometric ratio of 1:1.267 instead of 1:2. Significant peak broadening observed for samples synthesized using our protocol can be credited to (a) smaller crystallite size and (b) layered nature of hexagonal MoS_2. However, the sharpness of the peaks is better in MS21 than MS9 which may be due to better crystallinity due to longer reaction times.

3.2.2.2 Field emission scanning electron microscopy

FESEM images for the resultant powder are displayed in figure 3.3 (a)–(d). FESEM images of samples corresponding to 1:3 molar ratio of Mo salt and thiourea and with different reaction intervals (9 and 21 hr) illustrates the formation of molybdenum sulfide nanoscale hierarchical morphologies from basic building blocks such as sphere and rod-like structures. The FESEM image (low magnification) of the sample MS9 shows (figure 3.3a) spherical hierarchical marigold flower-like structures having a size in the range of 1 µm to 2 µm. At high magnification, as seen in figure 3.3b each marigold flower is made up of petal-like nanostructures. Each petal has thickness ~ 10-20 nm. Low magnification image corresponding to sample MS21 reveals hierarchical rod-like structures as shown in figure 3.3c. In this case, we can observe totally different morphology feature of above sample, i.e., like hornbeam flower having a size of 100-200nm. Each hornbeam flower is separated from each other. At high magnification (figure 3.3d), we can see the flower petals of thickness ~ 20-30 nm.

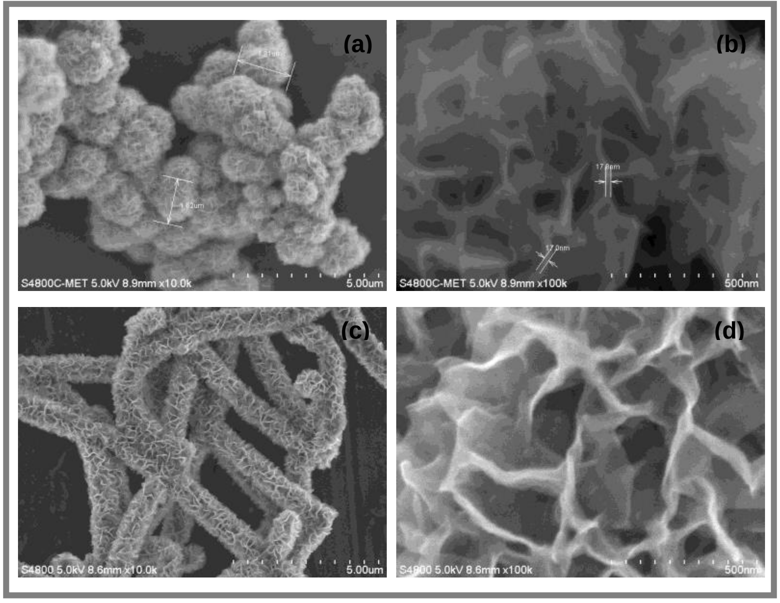

Figure 3.3 *FESEM images of the resultant nanostructures corresponding to samples MS9 (a) & b) low and high magnification) and MS21 (c) & d) of low and high magnification).*

3.2.2.3 Field emission transmission electron microsocpy

To ascertain the microstructure of the resultant powder, representative FETEM images of the resultant powders corresponding to MS9 and MS21 were obtained as shown in figure 3.4 and 3.5, respectively. The FETEM images disclose the predominant formation of flower-like nanostructures in the case of MS9 sample (figure 3.4a). At higher magnification, we could observe the petals which are fragile and appear to be made up of few layers of MoS_2 (figure 3.4b). The lattice image (figure 3.4c) shows that the petal at the twist is made up of around 20 layers with the d value as 6.2 Å which matches with the available reports of few layered thick MoS_2 nanostructures [12].

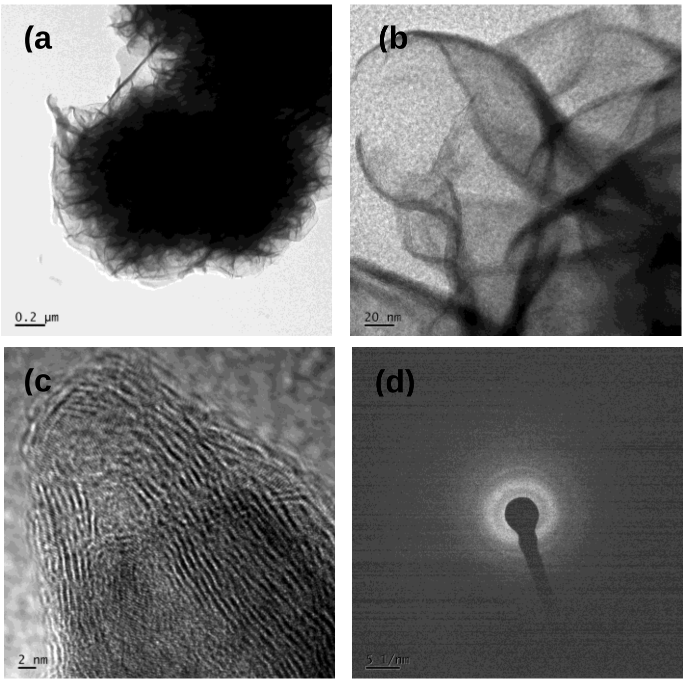

Figure 3.4 *FETEM image of the resultant MS9 sample a) low magnification, b) high magnification, c) lattice image and d) SAED pattern.*

In the case of the sample prepared at the reaction time of 21h (MS21), the low magnification FETEM image shows the formation of hornbeam flower-like structures (figure 3.5a). However, flower-like morphology appears to be distorted which may be attributed to ultrasonic agitation used for the FETEM sample preparation. However, from high magnification image (figure. 3.5b), it appears that the petals are thicker and are made up of many layers. In this context, it is worthwhile to note that MoS_2 belongs to the family of layered structures. Thus, more tendency to form sheet-like 2-D structures is observed. These flower petals like structures correlate well with the similar structures seen in FE-SEM images for this sample. SAED pattern reveals ring-like patterns indicating polycrystalline nature of the sample. However, pressure of spots it the rings disclose in nanocrystalline nature

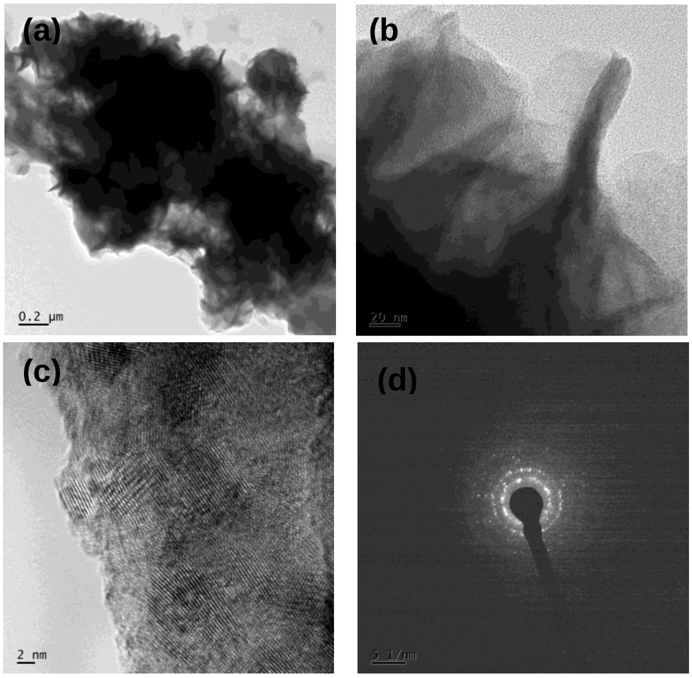

Figure 3.5 *FETEM image of resultant nanoparticle of sample MS21 a) low magnification, b) higher magnification, c) lattice image and d) SAED pattern.*

3.2.3 Summary

Synthesis of hierarchical nanostructures of MoS_2 has been accomplished using the hitherto unreported hydrothermal method. The prepared materials have a hexagonal structure. These hierarchical nanostructures have very high surface area due to the presence of petal-like surface features. Such high surface area nanostructures can be useful for applications like water splitting, pseudocapacitors, etc.

3.3 Synthesis of Molybdenum Sulfide Nanostructures (MSNs) via Microwave-Assisted Solvothermal Route

3.3.1 Experimental

3.3.1.1 Synthesis of MSNs

All the reagents were of analytical grade and were used as received without any further purification. In a typical experimental procedure, ammonium molybdate [$(NH_4)_6Mo_7O_{24}$. $4H_2O$] and elemental sulfur were mixed in 1:1 molar ratio in 10 ml hydrazine monohydrate ($NH_2NH_2{\cdot}H_2O$) and 30 mL deionized water (DIW) under magnetic stirring for 5 min. The resultant solvent mixture was transferred to Teflon vessel and subjected to microwave radiation of 270 Watt in a household microwave oven (Godrej GMC 30E) for 10 min, and subsequently, was allowed to cool down naturally to room temperature. Black precipitate settled at the bottom of the solution was filtered, washed with DI water, diluted hydrochloric acid and ethanol successively and centrifuged to remove the unreacted precursors. The final product was dried in vacuum oven at 50 °C for 4 h. The schematic describing the outline of the experimental work is illustrated in figure 3.6.

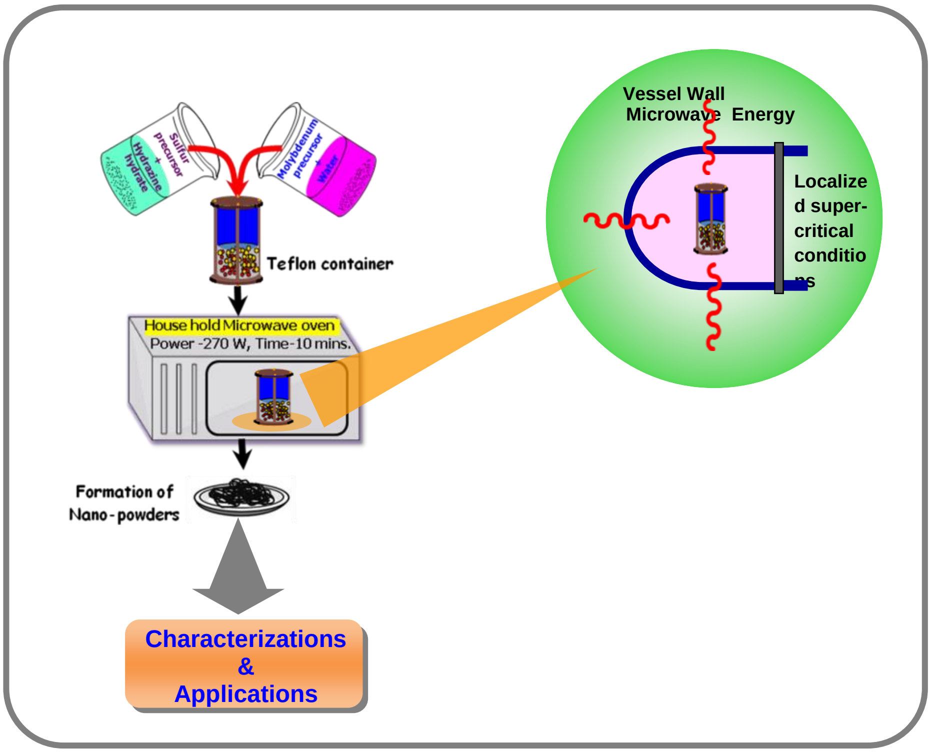

Figure 3.6 *Schematic of the reaction protocol for microwave assisted synthesis of* MoS_2 *nanostructures.*

3.3.1.2 Characterization of MSNs

The resultant samples were extensively characterized for their structural and morphological features by a variety of analytical techniques. Wide-angle X-ray diffraction (WAXD) analysis of our sample was accomplished for accurate phase identification by resolving the overlapping peaks using Philips X-Pert PRO Diffractometer. Field emission scanning electron microscopy (FESEM) was used to image as-prepared molybdenum disulfide sample using HITACHI S-4800. The resultant powder was directly put on the conducting carbon sheet without dispersing in any solvent and coated with conducting gold film. Dynamic light scattering (DLS) measurement was performed using 90Plus zeta sizer (Brookhaven Inc, NY) for measuring the hydrodynamic diameter of MSNs. MSNs were also characterized by AFM on an Agilent 5500 AFM/SPM microscope under acoustic AC mode using Si probes operating at a resonant frequency of 154 kHz. In all the AFM measurements, topography, phase, and amplitude images were obtained.

For clarity, only the topographic images were compared and presented. Field emission transmission electron microscopy (FETEM) was carried out for powder placed on carbon-coated copper grid (using a liquid dispersion of MSNs in isopropyl alcohol) using JEOL JSM 2100. Raman spectra were obtained at room temperature on a Horiba JY Lab RAM HR800 micro-Raman spectrometer with 17mW and 632.8nm laser excitation (He-Ne laser, E_{laser} =1.96eV) in backscattering mode. UV–Vis DRS spectra of powder sample was taken using a JASCO, V-670, UV–Vis–NIR spectrophotometer. The X-ray photoelectron spectra (XPS) were acquired using VG Scientific, UK, ESCA-3-MK-II electron spectrometer with Mg K_{α} (1253.6 eV) radiation.

3.3.2 Results and discussion

3.3.2.1 X-ray diffraction

The synthesis of MSNs was carried out via microwave assisted solvothermal technique reported for other materials [13]. Microwave-assisted solvothermal technique qualifies for the energy efficient ‘greener’ approach to drastically reducing the reaction time (~300 times faster than the conventional method). Microwave radiation penetrates through Teflon vessel and interacts with the solvents directly causing localized heating and thus generates supercritical conditions favorable for nucleation and growth of nanoparticles. XRD results show the tendency of these particles inclining towards amorphous nature in figure 3.7a. Wide-angle X-ray diffraction (WAXD) analysis of our sample was accomplished for accurate phase identification by resolving the overlapping peaks using Philips X’Pert PRO Diffractometer (figure 3.7b). The major diffraction peaks are characteristic of hexagonal MoS_2 (JCPDS # 24-0513). The presence of the second phase viz. hexagonal $Mo_{15}S_{19}$ is confirmed by standard finger-printing with the reported data (JCPDS # 40-0936) as a minor phase. WAXD results disclose that synthesized powder exhibits symbiotic existence of biphasic compound comprising MoS_2 and rarely occurring $Mo_{15}S_{19}$. The diffraction peaks are the very wide entailing presence of nanoscale crystallites. The crystallite size can be calculated using Scherrer’s equation 3.1 given as [14]:

$$T = K \lambda / \beta \cos\theta \quad \text{-------------------}[3.1]$$

Where,

T=crystalline size,

K=constant,

β= full width at half maximum (FWHM) of the diffraction peak

θ =angle of reflection.

The average crystallite size calculated using Scherrer's equation is in the range of 1–3 nm.

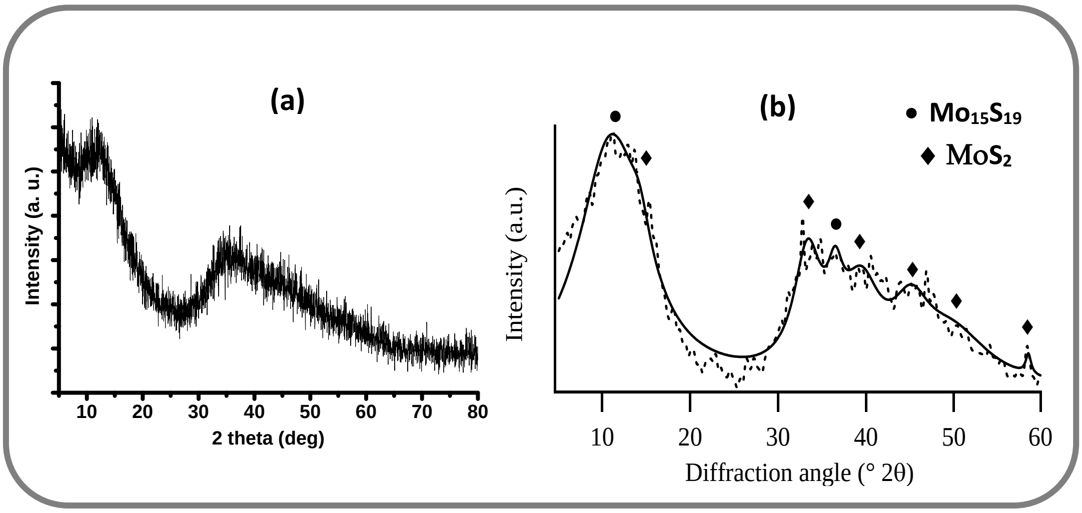

Figure 3.7 *a) XRD pattern and b) WAXD pattern of resultant molybdenum sulfide powder revealing biphasic nature. The dashed trace and continuous line depict the experimental pattern and fitting function in figure.3.7b, respectively.*

3.3.2.2 Field emission scanning electron microscopy , dynamic light scattering and atomic force microscopy

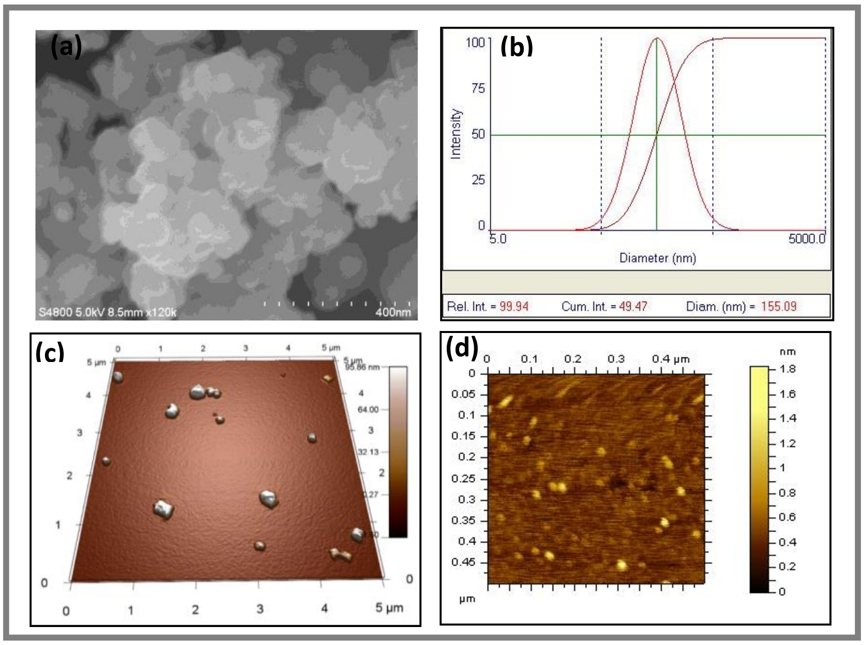

Figure 3.8 *Surface morphology and particle size determination. a) FE-SEM image of resultant MoS_2 powder. b) DLS particle size measurement of MSNs after filtering using 0.2 lm syringe filter. c) AFM image of MSNs at low magnification and d) representative topographic image at 0.5 x 0.5 µm area image of MSNs*

FESEM image reveals the formation of spherical and irregular shaped particles which (figure 3.8a) appeared to be agglomerated and few irregular shaped plate-like structures appear to be stacked one above the other. Sizes of these structures vary from 40 to 150 nm.

The DLS measurements showed an average intensity weighted particle size ~583 nm. The DLS measurement provides the hydrodynamic size and is expected to be larger than the physical size measured by other techniques such as transmission electron microscopy. Moreover, if the sample is non-homogeneous and a few larger sized nanoparticles are present in the sample, the measurement is skewed towards the larger size. Hence, in this case, the particle size of MSNs was significantly bigger than that of obtained by HRTEM. Therefore, particle size was measured again after filtering the above samples using a 0.2 µm syringe filter. A significant change in the particle size measurement was noted which is reduced to ~ 155 nm (figure 3.8b). This size is more consistent with what is expected by TEM measurement. The AFM measurements of MSNs helped to elucidate the morphology along with the size. A representative image in Figure 3.8c shows some large aggregated particles in size range of 200-400 nm.

The height of these particles is in the range of 100 nm. This indicates that these MSNs are not spherical but have a plate-like structure. However, for the 0.5x0.5 µm image, several smaller sized nanostructures are seen having size ~ 20 nm and the average height of 2 nm (figure 3.8d). The obtained morphology is consistent with the larger-sized aggregates regarding plate-like structure. The AFM results are consistent with the particle size measurement by DLS method.

3.3.2.3 Field emission transmission electron microscopy

FESEM image (figure 3.8a) reveals the formation of spherical, irregular shaped particles at the nanoscale; however, XRD results show the tendency of these particles inclining towards amorphous nature. Therefore, in order to identify the exact morphological structure of synthesized nanostructure, FETEM imaging (i) before ultrasonication and (ii) after ultrasonication (for 5 minutes in isopropyl alcohol) was accomplished as a display in figure 3.9 (a) and (b). The FETEM image of the sample before ultrasonication discloses similar morphology as obtained in FESEM showing spherical and irregular shapes (50-100 nm). Nevertheless, surprisingly after ultrasonication, the particles appear to disintegrate forming smaller elongated rod-like morphological structures (10-20 nm). This result indicates that even though as prepared particles appear bigger in size, they may be made up of smaller rod-like structures bundled to each other with weaker bonds. Ultrasonication is sufficient to break their weak bonding leading to the formation of smaller structures which do not have a long range crystalline order which consistent with is observed in XRD results. The corresponding SAED pattern shows diffused ring-like structure with few spots indicating the presence of little crystallinity. Lattice image (figure 3.9c) shows moderate crystalline nature which can be correlated with substantial peak broadening as observed in WAXD. Two such crystalline regions of the sample are depicted in figure 3.9 (d & e), respectively which corresponding to a d value of 2.27 Å.

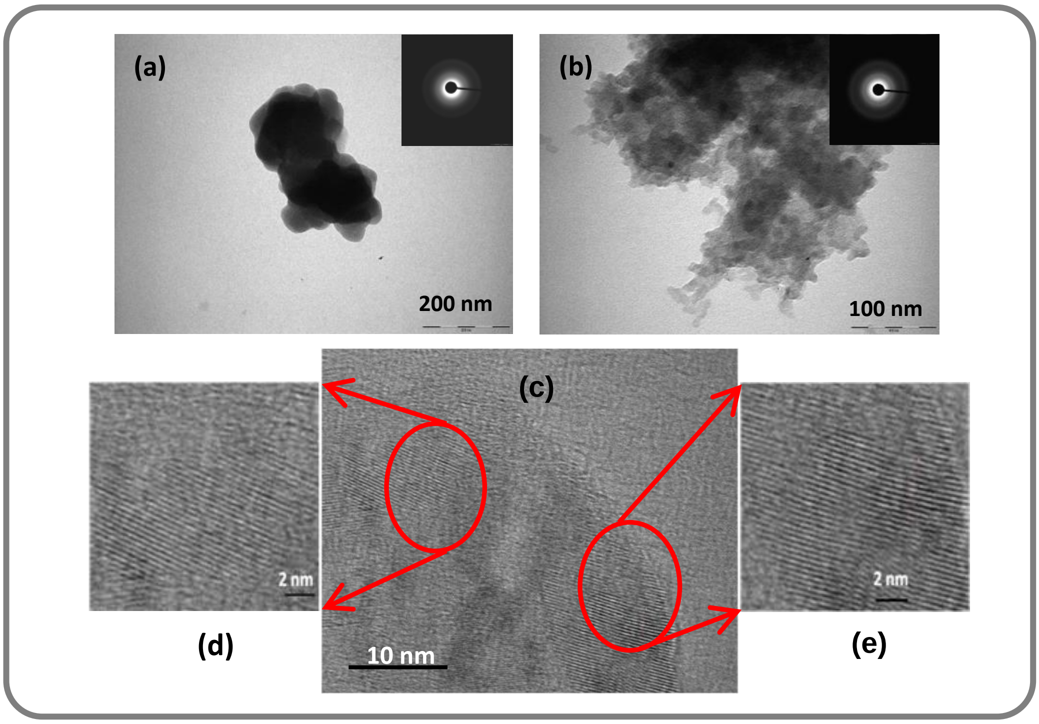

Figure 3.9 *TEM images of resultant molybdenum sulfide nanopowder at (a) without ultra-sonication and (b) with ultra-sonication. Lattice image of the sample (c) with enlarged crystalline regions displayed in (d) and (e).*

3.3.2.4 Raman spectroscopy

Raman spectrum of the resultant molybdenum sulfide powder is depicted in figure 3.10a. Peaks corresponding to E^2_{2g} (32 cm^{-1}), E_{1g} (286 cm^{-1}), E^1_{2g} (383 cm^{-1}) are observed which correspond to MoS_2, while peak at 408 cm^{-1} (A_{1g}) is missing [15]. In the same way, other three more peaks can be assigned to the terminal oxygen (Mo=O) stretching mode at 995 cm^{-1}, the triply-connected bridge-oxygen (Mo_3-O) stretching mode at 665 cm^{-1}**,** and the doubly-connected bridge-oxygen (Mo_2-O) stretching mode at 818 cm^{-1}, respectively, which can be attributed to molybdenum oxide [16]. MoS_2 has a high probability of being burned by the laser beam (even at low beam power) if examined in the air by laser Raman spectroscopy, and then they may display only the MoO_3 spectrum [17]. In the present Raman investigation, highest intensity peaks observed at 818 and 994 cm^{-1} corresponding to MoO_3 may also be attributed to the burning of MoS_2 which leads to its transformation into MoO_3. Nevertheless, peaks at 60.2, 80.6, 95.2, 112.7, 124.5, 147.8, 195, 212, 238, 338 and 464.1 cm^{-1} cannot be associated with either MoS_2 or MoO_3. It is speculated that some of these above peaks may belong to $Mo_{15}S_{19}$, but the pertinent data is not available in the literature. Peaks broadening indicate that the corresponding vibration modes are due to a structure with less crystallinity.

3.3.2.5 UV-visible spectroscopy

The UV-visible spectrum of resultant molybdenum sulfide nanopowder is shown in figure 3.10b. Bulk MoS_2 shows optical spectra with indirect band gaps of 1.23 eV (absorption edge of 1040 nm) and 1.69 eV, respectively [18]. As a semiconductor, it demonstrates the relationship between band gap and particle size. In figure 3.10b, a broad absorption hump centered around 500 nm is observed, which shows large blue shift (from ~ 1040 nm to 500 nm) due to quantum size effect. The broadness of the hump may be attributed to the wide particle size distribution which is further evinced from FESEM image. Formation of the well-defined band gap is impaired due to reduced crystallinity of the material. Hence, the resultant sample may not be optically interesting; however, it may enhance the catalytic activity due to availability of a large number of active edge atom sites [19].

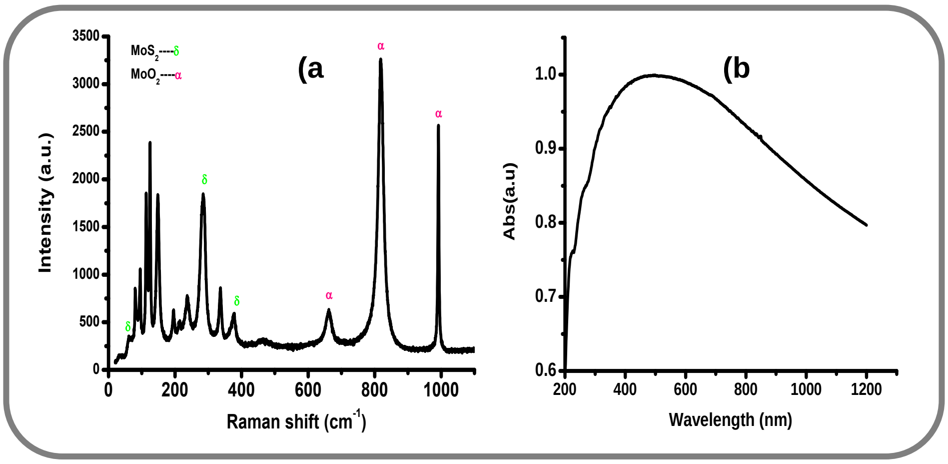

Figure 3.10 *(a) Raman and (b) UV-Vis spectrum of the resultant MSNs.*

3.3.2.6 X-ray photoelectron spectroscopy

Further understanding of the chemical composition was accomplished by the X-ray photoelectron spectra of the resultant sample which are displayed in figure 3.11. The C 1s binding energy of carbon contamination occurs at 284.3 eV. The binding energies of Mo ($3d_{5/2}$) and Mo ($3d_{3/2}$) in the sample of MSNs were observed at 232.5 and 229.5eV, respectively (figure 3.11a). The binding energies of S ($2p_{3/2}$) and S ($2p_{1/2}$) in the sample of MSNs were spotted at 161.6 eV and 162.7 eV, respectively (figure 3.11b). From XPS, an inference can be drawn about the presence of well-defined spin coupled Mo and S doublets at binding energies which are consistent with the values of molybdenum disulfide [20].

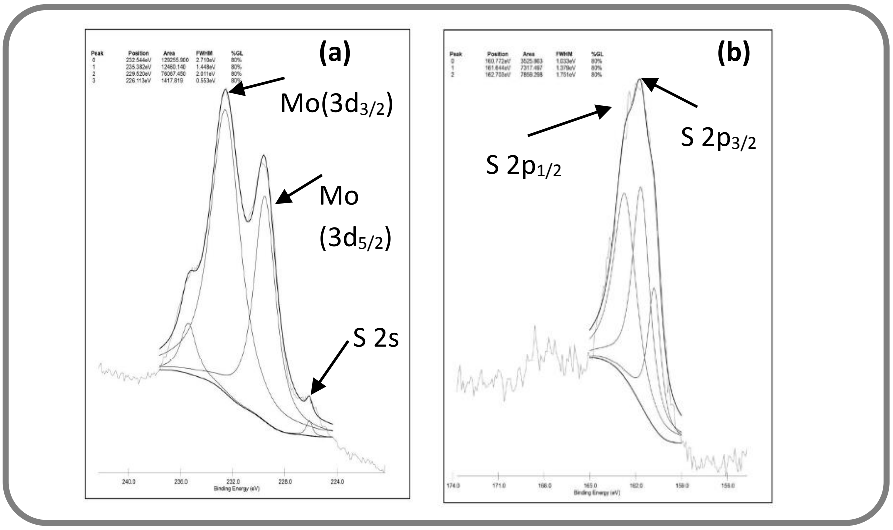

Figure 3.11 *High-resolution XP spectra of resultant MSNs a) Mo 3d spectrum and b) S 2p spectrum.*

3.3.3 Antimicrobial activity assay

3.3.3.1 Introduction

Indiscriminate use of antibiotics against infectious diseases is turning out to be a vicious cycle of developing new antibiotic drug and its resistant strains in short time span due to the inherent tendency of microbial cells to alter their genes. The origin of the multidrug resistant (MDR) microbes lies in the increased evolutionary selection pressure on microbial population which allows the resistant microbes to survive and the susceptible ones to perish. Antibiotic resistance, therefore, poses a significant healthcare threat. There is an urgent and compelling necessity for making improvements in present methods and develop novel strategies to tackle the situation. Three possible solutions emerging in this context are (1) generic approach for the development of conventional and newer antibiotics based MDR drugs. This approach may not be feasible for the longer period as there may be a possibility of bacterial resistance to such drugs. Nevertheless, nanomaterials may prove useful in designing the next two approaches, namely, the (2) bactericidal (contemporary) approach of exploitation of inorganic nanoparticles to develop antiseptics that are deadly to microbes and may demonstrate wide-ranging activity and lower prospect to promote microbial resistance. However, many nanoparticles have different degrees of toxicity causing restrictions in their use directly as antibacterial agents [21], and (3) bacteriostatic approach which is the least explored but is significantly emerging and promising. Under this approach, nanomaterial can be applied as an agent that inhibits the formation of biofilms without actually killing the microbial cells. Biofilm growth can cause infection [22] and has detrimental effects on various materials and equipment like medical devices, implants, and food-processing equipment, thereby causing enormous economic and health-related damages [23]. It may be noted that in the context of drug-resistant strains and ineptness of traditional treatments, the nanomaterial based approaches do not exert evolutionary pressure on bacteria and hence can be beneficial in the long run. Nanoparticles, especially metallic ones, tend to offer an effective solution for overcoming bacterial resistance [24]. But, metallic nanoparticles have different degrees of cytotoxicity, which restrict their use in antimicrobial drugs. In this explicit perspective, we have stumbled upon the report pertaining to biocompatibility and non-cytotoxicity of molybdenum disulfide nanoparticles [25]. However, they cannot be claimed as complete antimicrobial package unless and until their capabilities showing profound antimicrobial activity and/or anti-biofilm ability are established. Molybdenum disulfide belongs to a family of fundamentally and technologically important multifunctional layered materials. It forms sandwich interlayer structure created by S–Mo–S layers, which are loosely bound to each other only by van der Waals forces [26]. Such structures, at the bulk and nanoscale, exhibit a broad array of applications, such as electrochemical hydrogen storage [27], cathode material for rechargeable lithium batteries and solar cells [28, 29], electric transport [30], useful solid lubricant [31], an intercalation host [32], and field emission tips [33]. For example, molybdenum disulfide may be an alternative material for next-generation nanoelectronic devices viz., transistor [34] and tandem photovoltaic configurations, because its electronic properties are superior to silicon [35] and its band gap, transforms from indirect to direct at the nanoscale. So far, nanoscale molybdenum disulfide has been obtained with different morphologies such as hollow microtubes and microspheres [36, 37], amorphous tube-and ball-like structures [38], nano-wires [39], randomly stacked layers [40], etc. for a host of applications. However, synthesis of molybdenum disulfide nanostructures (MSNs) using a facile and 'green' technique is still a prime challenge which is certainly advantageous from the standpoint of futuristic nano-biotechnology based (including antimicrobial) applications. In this section of the chapter, we present an expedient and 'green' microwave assisted solvothermal synthesis [24] of MSNs and hitherto unreported pre-therapeutic antimicrobial application protocol of the same. Fundamentally, the synthesized products were explored for antimicrobial applications with two-pronged intentions: (1) to probe biofilm inhibition (in *Pseudomonas aeruginosa* PA 01) which is the earliest assertion of MSNs as anti-biofilm agents and (2) to assay the antibacterial property of synthesized nanoparticles (using model organisms, gram-positive *Bacillus subtilis* NCIM 2063 and gram-negative *Escherichia coli* NCIM 2931 and corroborate the possible mechanism by detecting and measuring the reactive oxygen species (ROS) and simultaneously monitoring the redox enzymes. Additionally, non-cytotoxic nature exhibited by MSNs in the case of Hela cells boosts their scope as anticarcinogenic material.

3.3.3.2 Experimental

3.3.3.2.1 Antimicrobial activity assay

Determination of minimum inhibitory concentration (MIC) / minimum bactericidal concentration (MBC)

The as-synthesized MSNs were dispersed as a colloidal suspension in sterile distilled water by sonication before testing for antimicrobial activity. All *in-vitro* antimicrobial activity study was performed using gram positive and negative model organisms viz. *Bacillus subtilis* NCIM 2063 and *Escherichia coli* NCIM 2931, respectively. MIC and MBC are the lowest concentrations (of nanoparticles, in the present case) at which a tested compound, respectively, inhibits growth or kills more than 3log (99.9%) of bacteria. Since the as-synthesized MSNs in Mueller–Hinton (MH) medium form a suspension, rather than solution, MBC results were recorded by calculating the colony forming units per milliliter (CFU/mL). In short, a 24-well microtiter plates containing one mL MH broth (Hi-Media

Mumbai, India), with nanoparticles (in the concentration range of 37-1000 µg/mL) were inoculated with test strains (final cell density of 5 × 10^4 CFU/mL) and incubated at 37 °C for 15 h. The lowest concentration of nanoparticles showing visual growth inhibition was considered as the MIC. The MBC was measured by preparing serial dilutions from the MIC assay and plating the dilutions on MH agar plates. The data were recorded as survival rates (CFU/mL), based on 100% survival for the untreated control. All MIC and MBC values reported were based on three experimental repeats [41].

Biofilm assay

P. aeruginosa PA 01 was grown overnight in Luria-Bertani (LB) medium at 37°C with agitation. After growth, the culture was diluted with LB medium (OD600 0.02), and 50 µL of the diluted culture was added to 950 µL of LB medium supplemented with 150 µg/mL of MSNs and were incubated statically for 18 h at 37 °C in 8 well glass chamber slide. After incubation, planktonic bacteria were discarded, and the biofilms were washed three times with cacodylate buffer (CB, 0.1M, pH 7.4). Biofilms formed on glass plates were fixed in 2 % glutaraldehyde using 0.1 M CB (pH 7.4) for 4 h at 4 ˚C. After thorough washing with CB, samples were dehydrated in a series of ethanol solutions (10–100 %). The samples were dried, mounted on aluminum stubs with conductive carbon cement, and finally coated with a gold film for observation under FESEM (Hitachi 4800 SEM at 1.5 kV) [42]. For CLSM, after initial through washing, the biofilm was covered with 50 µL of 100 µg/ml of dye, concanavalin A, Alexa flou r 488, and incubated for 30 min at 4 ºC. The biofilm was finally washed with cacodylate buffer of 0.1M, pH 7.4, and observed under fluorescence microscopy (Zeiss, Germany) with an excitation of the wavelength of 488 nm and emission at 519 nm [43]. The statistical analysis was also performed by using Image Quanta Analysis (Zies, Germany).

Detection, Measurement of ROS and Determination of Cell morphology

The ROS generated by the action of MSNs inside the cells were fluorometrically assayed by fluorescence microscopy while its morphology is detected by FESEM. In a typical experimental procedure, the cells of *B. subtilils* and *E. coli* were grown to mid-log phase ($1x10^7$ cells/mL) and then treated with MSNs (MIC_{50} value, i.e., the value where

50% reduction in the viable cells takes place) for 3 hrs at 37 °C and 150 rpm. The cells were collected by centrifugation at 10000 rpm for 15 mins at 4 ^{0}C [44].

Fluorescence Microscopy

The cell pellets were washed 3 times with 0.1 M phosphate buffer (PB) at pH 7.4 and incubated with 25 µM DCFH-DA for 30 min. At the end of the incubation, cells were washed with phosphate-buffered saline (PBS) again. The fluorescence of 2',7'-dichlorofluorescein (DCF), which is the oxidized product of hydrolyzed 2',7'-dichlorofluorescein (DCFH, from DCFH-DA by intracellular esterases), was detected by observing the cells under microscope (Zeiss) at 1000X magnification and measured with a Varian fluorescence spectrophotometer, using excitation and emission wavelengths of 485 nm and 530 nm, respectively. The DCF concentration in cells not exposed to nanoparticles was used as a control.

Scanning Electron Microscopy

The cell pellets were washed 3 times with 0.1 M PB at pH 7.4, and fixed in PB containing 2.5% glutaraldehyde at 4^{o}C for 4h. After rinsing twice with PB, the pellets were dehydrated in ethanol serials (10%, 30%, 50%, 70%, 80%, 90%, and 100%, 15 min per step), and then dried in air.

Extraction of Proteins and Assay of Antioxidant Enzymes

For the extraction of proteins, 300 mL MH broth was added with MIC$_{50}$ value (0.15mg/ml) containing MSNs and 5.0 x 10^6 cells of *B. subtilis* and incubated till the density reached to mid-log phase (4 h), upon which it was centrifuged at 10000 rpm for 15 mins at 4 ^{0}C. The cell pellets were suspended in cell lysis buffer (PB, 0.1 M, pH 7) and subjected to sonication (10 kHz for 8 min with four intervals of 2 min each) in ice-cold condition (4 ^{0}C). The sonicated sample was centrifuged at 15,000 rpm for 30 min at 4 ^{0}C, and the resulting supernatant was used for the assay of antioxidant enzymes. The protein extracted without using nanoparticles was used as a control. Total SOD activity was assayed by monitoring the inhibition of reduction in nitro blue tetrazolium (NBT). The reaction mixture of 1ml contained 50 mM potassium phosphate buffer (pH 7.8), 13 mM methionine, 75 µM NBT, 2 µM riboflavin, 0.1 mM Na_2EDTA, and known volume (µL) of enzyme extract corresponding to 250 µg of proteins [45]. The reaction mixture was illuminated, perpendicularly, for 15 min under 60 W fluorescent tubes at a distance of 10 cm. One unit of

SOD activity was defined as the amount of enzyme required to cause 50% inhibition of NBT reduction monitored at 560 nm. Catalase activity was determined by measuring the consumption of H_2O_2 (extinction coefficient 39.4 mM^{-1} cm^{-1}) at 240 nm for 1 min by the method of Aebi. The reaction mixture contained 50 mM potassium phosphate buffer (pH 7.8), 10 mM H_2O_2, and known volume (µL) of the enzyme extract corresponding to 100 µg of proteins in 1 ml volume (Abei 1984).

Cytotoxicity Study

The cytotoxicity of the MSN against HeLa cells was evaluated by observing cells under a microscope and determining the metabolic activity by 3-[4,5-dimethylthiazol-2-yl]-2,5 diphenyl tetrazolium bromide (MTT) assay. Briefly, cells were seeded into a 96-well culture plate at $2X10^4$ cells/well in a 100 µL culture medium. After incubation at 37 °C in a 5% CO_2 incubator for 24 h, cells were exposed to the 300 µg/mL of MSN. The cells were incubated for 72 h, followed by the observance of cells morphology under the microscope at 40X magnification (Zeiss, Germany). For MTT assay, cells were washed in 0.1M PB saline, added with 20 µL of MTT solution (5 mg mL^{-1}) and incubated in the dark for 3 h. 100 µL of DMSO was added to wells and absorbance was recorded at 550 nm in a microplate reader (Thermo-Fisher, USA) and further cultivation for 4 h.

3.3.3.3 Result and discussion

3.3.3.3.1 Biofilm inhibition in *P. aeruginosa* via the effect of MSNs

FESEM analysis of biofilm (corresponding to *P. aeruginosa*) treated with our MSNs (at a concentration of 150 µg/mL) was performed to ascertain its morphological appearance. *P. aeruginosa* was specifically used as a model organism in studying the formation of biofilm on account of its dreadful nuisance in hospitals, particularly, in skin burns. When cells of *P. aeruginosina* were grown in the presence of nutrient medium, they adapt to grow, multiply and communicate to each other by generation of quorum, and upon reaching the critical level density of quorum, they start formation of web-like structure consisting of dense polysaccharides with cells and their debris embedded inside (a biofilm).

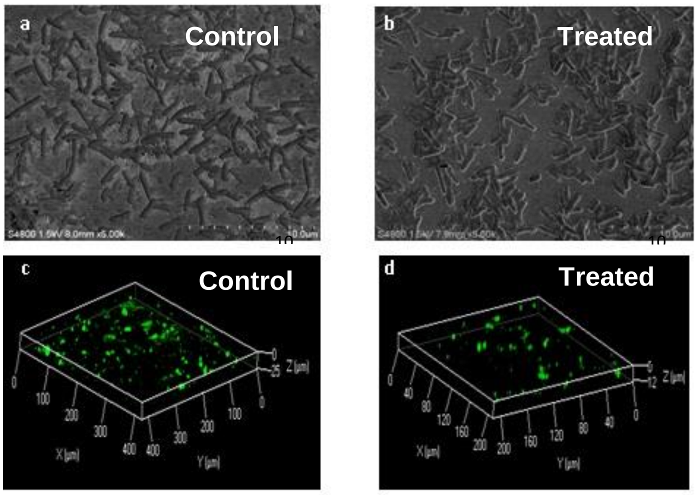

Figure 3.12 *Biofilm inhibition effect and CSLM analysis. Representative FESEM image showing effect of MSNs treatment on biofilm inhibition in P. aeruginosa a) Control, web-like structure beneath the cells is biofilm and b) MSNs treated, weblike structure is diminished. Under Confocal microscopy, biofilm of P. aeruginosa PA 01. c) Control, a typical biofilm, and d) MSNs treated, a truncated formation of biofilm*

The free suspended cells are called as planktonic. In sample prepared without MSNs treatment (control), a web-like mass underneath the cells was observed, a typical indication of biofilm structure (figure 3.12a), whereas, for MSNs treated sample, exposed cells with significantly diminished biofilm underneath are observed (figure 3.12b). The diminished biofilm in MSN treated *P. aeruginosa* was not due to the inhibition of the growth of planktonic cells as the number of planktonic cells in the MNS treated cells were nearly same as in control. When we assayed the number of planktonic cells in MNS treated samples and control, it was nearly equal, approximately, 2.3 x 10^7 cells/mL. Confocal scanning laser microscopy (CSLM) analysis also confirmed impedance in biofilm formation in the presence of MSNs (figure 3.12c and d). Under CSLM, biofilms were seen with patches of fluorescence (figure 3.12c), a typical of biofilm. However, in the presence of MSNs (figure 3.12d), the fluorescence was spatially distributed, indicating truncated formation of biofilm (decrease by about 40%). In addition, shrinkage in depth of biofilm after MSNs treatment, in comparison to control, can be clearly observed. In comparison to control, the shrinkage in the depth of biofilm was about 12.5 µm (S.D 0.05). Various nanoparticles have been reported as agents inhibiting the formation of biofilm, however, intriguingly, most of these nanoparticles displayed this property owing to inhibition of cell growth [46]. However, our MSNs impede the formation of biofilm in *P. aeruginosa* without actually disrupting bacterial cells or their function (As FE-SEM evidence in figure 3.12a & b). The possible reason for such behavior would be the inhibition of quorum sensing (QS) phenomenon. The QS is a phenomenon in which organisms tend to communicate with each other by secreting a sense molecule into the surrounding medium. When the cell density of *P. aeruginosa* reaches to a critical level, they tend to form a biofilm. Nevertheless, we speculate that MSNs somehow interfere this QS phenomenon, and thus, inhibit biofilm formation. Growths of the planktonic cells are not inhibited as the concentration used was insufficient to hinder the metabolic reactions inside cells. Peculiarly, the inhibition of biofilm formation by our MSNs is significant as biofilm protects the pathogenic organisms from drugs and immune system by resisting entry and recognition, respectively. Thus, our MSNs can also be regarded as a potential candidate in treating biofilm-protected infections and prevent any bacterial colonization on medical devices implanted in tissues of a human being.

3.3.3.3.2 Assay on bactericidal activity of MSNs

MIC (the minimum concentration of which a visual inhibition of growth) of MSNs against *B. subtilis* and *E. coli* were 300 µg/mL and 1000 µg/mL, respectively. Interestingly, the MBC value too was 300 µg/mL (figure 3.13a) and 1000 µg/mL (figure 3.13b) against *B. subtilis* and *E. coli*, respectively. In comparison to *B. subtilis*, a higher value of MBC (lower activity) of MSNs in *E. coli* is due to the presence of an outer layer of lipopolysaccharides. The outer layer of lipopolysaccharides is an extra protective layer in *E. coli*, which either hinder the entry of MSNs or absorbs the free radical generated on the cell wall of these organisms. The antibacterial activity of MSNs is striking especially because there are very few reports pertaining to metal-sulphide nanoparticles exhibiting antimicrobial activity [47, 48] and none for MSNs.

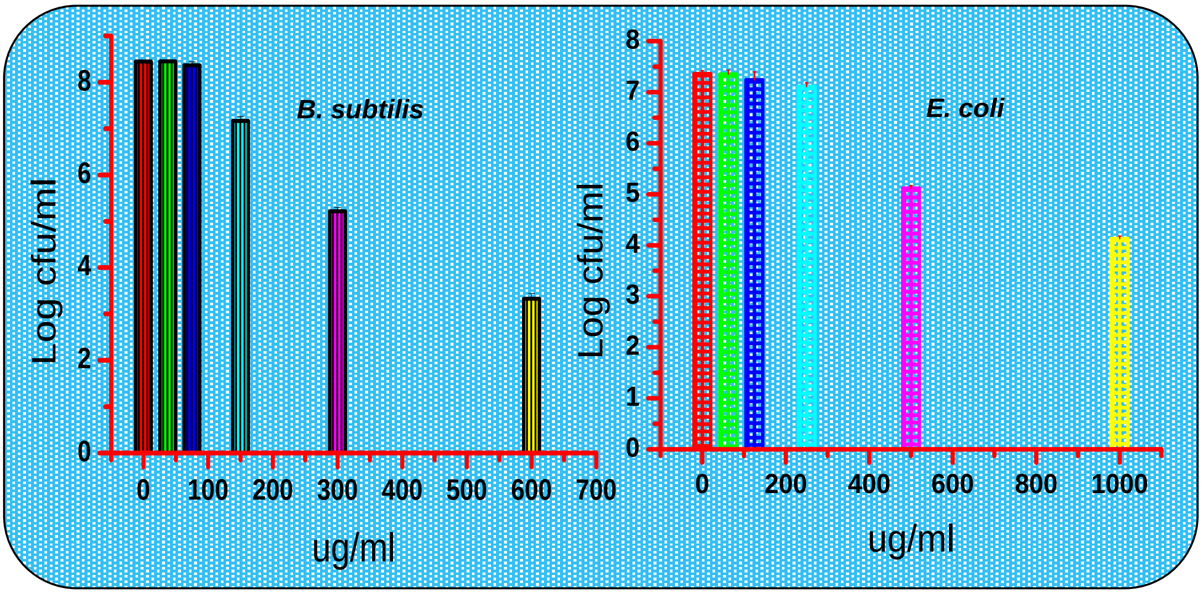

Figure 3.13 *Minimum Bactericidal Concentration (MBC) of as-synthesized MSNs against (a) B. subtilis @ 300 µg/ml and (b) E. coli @ 1000µg/ml*

In order to probe the possible bactericidal mechanism of MSNs, we carried out the quantitative determination of ROS generation in *B. subtilis* and *E. coli* cells treated with by fluorescence microscopy and spectrofluorometry (figure 3.14a). During this assay, hydrophobic 2',7'-dichlorofluorescein-diacetate (DCFH-DA) molecules, which readily penetrate cellular membranes, are hydrolyzed by intracellular esterases to yield DCFH, a non-fluorescent compound; DCFH is then oxidized by ROS to a fluorescent compound, 2',7'-dichlorofluorescein (DCF). A relatively lower generation of ROS in the case of *E. coli* in comparison to *B. subtilis* in the presence of MSNs particle is due to the presence of an outer envelope in *E. coli* (figure 3.13a). As higher reportier of ROS is generated inside *B. subtilis*, we decided to continue further studies with *B. subtilis*. The generation of ROS in cells of *B. subtilis* was corroborated by investigating the specific activities of redox enzymes, superoxide dismutase (SOD) and catalase (CAT). SOD is the first enzyme to interplay in the antioxidant mechanism that catalyzes the dismutation of superoxide anion radical (O_2^-) into oxygen and hydrogen peroxide. An increase in the specific activity is an indicator of increase in the biosynthesis of the enzyme. In the present study, the specific activity of SOD for samples treated with MSNs has enhanced from 0.88 (control) to 3.02 IU, a 3.45 fold increase (figure 3.13b). A 3.45 fold increase in specific activity is the clear indication of generation of (O_2^-) inside the cells of *B. subtilis* which has also been reported as the mechanism of tolerance to oxidative stress by TiO_2 in marine abalone i.e. *Haliotisdiversicolor supertexta* [49]. CAT is an important cellular defense, catalyzing the conversion of hydrogen peroxide (H_2O_2) to water (H_2O) and molecular oxygen (O_2).

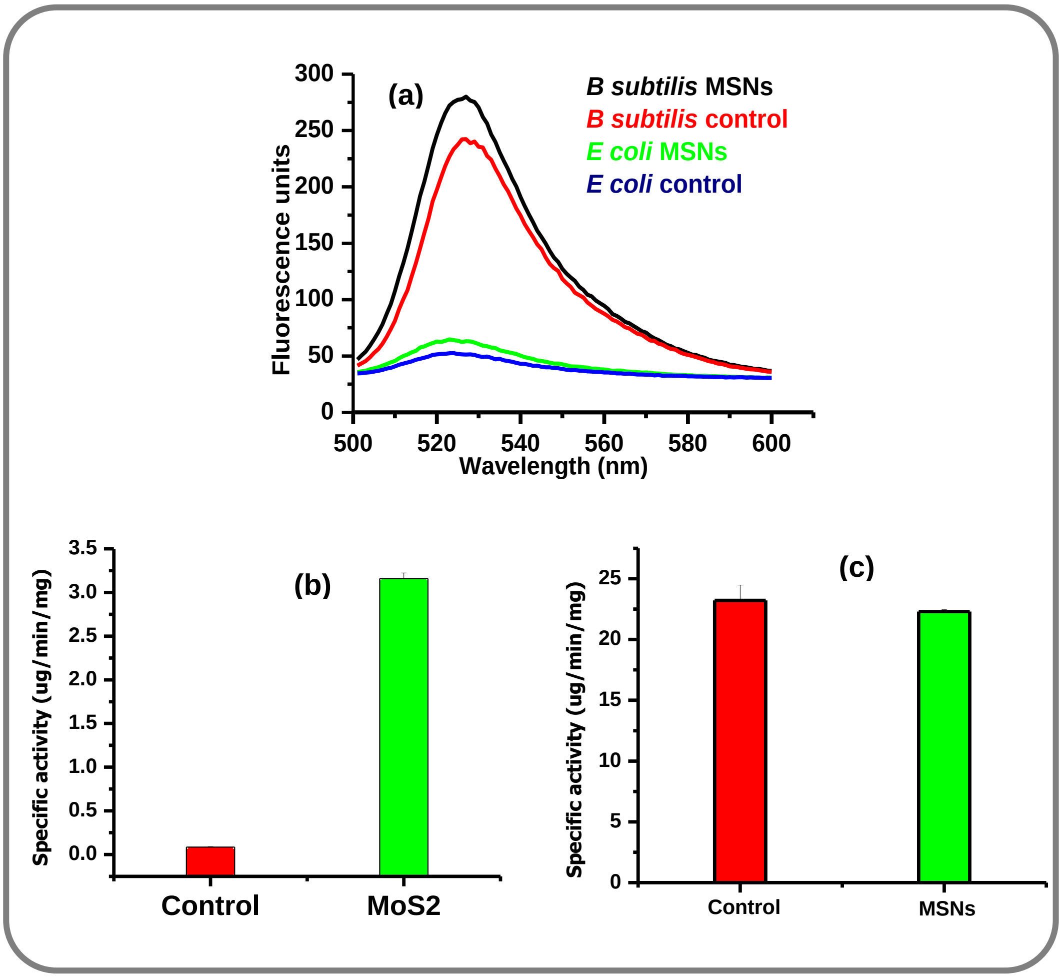

Figure 3.14 *(a) Measurement of ROS generation in fluorescence units. Redox enzyme activity via the specific activities of superoxide dismutase (b) and catalase (c) of B. subtilis in presence of MSNs.*

Since there was no change in activity of CAT in the presence of MSNs in *B. subtilis* (figure 3.14c), the antibacterial activity can be linked with accumulated $H_2O_2^-$ the dominating species in antibacterial action against various bacteria [50, 51].

Reported studies on interaction of nanoparticles with bacterial cells have suggested two main possible reasons for antibacterial activity: (i) generation of ROS [52] attacking the cytoplasmic membrane of bacteria and rupturing the cells and (ii) disruption and disorganization of membranes and/or disruption of cellular function due to deposition/accumulation of nanoparticles on surface of bacteria, in the cytoplasm or in the periplasmic region [53].

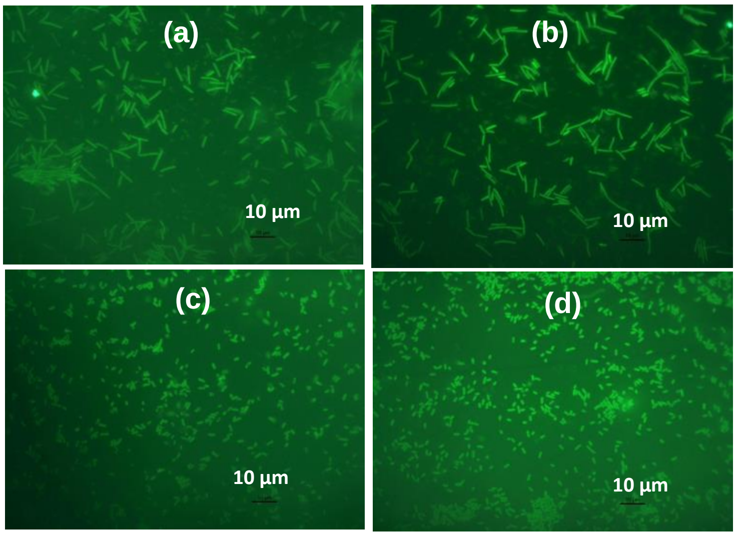

Figure 3.15 *Fluorescence microscopy (using H_2DFFDA staining for control) images of B. subtilis (a) Control and (b) treated and E. coli (c) control and (d) treated for determination of cell morphology during ROS generation.*

Therefore, in order to test the first hypothesis, fluorescence microscopy images of the cells were captured cells (figure 3.15 a-d) during ROS generation. A relatively higher fluorescence in images of both *B. subtilis* (figure 3.15b) and *E. coli* (figure 3.15d) as compared to their respective controls has been observed (figure 3.15a and 3.15c). Quite intriguingly, cell morphologies were found to remain intact as against the general trend of cell rupture.

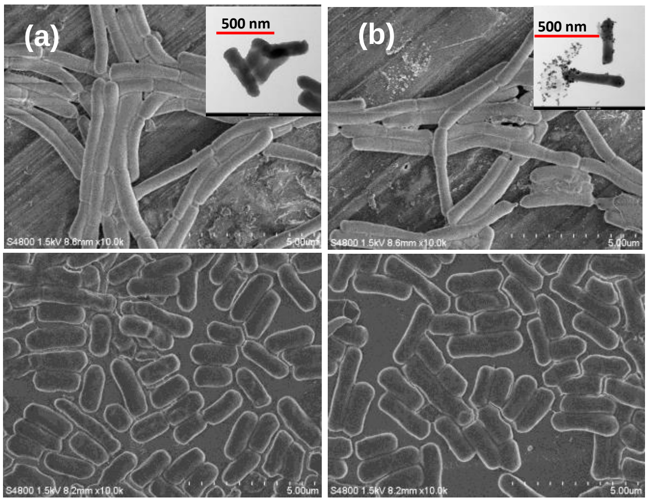

Figure 3.16 *FESEM images of B. subtilis and E. coli for cell morphology determination. (a) B. subtilis and (b), E. coli showed less fluorescence and for MSNs treated. (c) B. subtilis and (d) E. coli, a green fluorescence was detected. (Inset: TEM images for B. subtilis: control and treated)*

Therefore, in order to probe this phenomenon further, FESEM for *B. Subtilis* and *E. coli* and TEM images for *B. Subtilis* have been obtained (figure 3.16). FESEM images corresponding to *B. subtilis* (figure 3.16b) and *E. coli* (figure 3.16d) indicated that there was no rupture of cells, and cell morphologies remained intact like corresponding controls (figure 3.16a and 3.16c), in turn, ruling out possible rupture of the cells by ROS [54]. Transmission electron microscopic (TEM) observation of cells of model organism further corroborated SEM results that there is no cellular rupture (an insert in figure 3.16a & b). Thus, we conjecture that generated ROS act on *B. subtilis* and *E. coli* by yet unknown mechanisms of disruption of cellular function (most probably via damage to DNA, lipids, or proteins instead of cell wall rupture) in stark contrast with antimicrobial action of various nanoparticles as comprehended. The apparent mechanism of bactericidal action of MSNs based on the proposed hypothesis is shown schematically in figure.3.17. It may be noted that MBC values for *B. subtilis* and *E. coli* (at 300 µg/mL and 1000 µg/mL, respectively) after MSNs treatment in the present study seems higher since we used complex media for assaying antimicrobial and antibiofilm activity. We preferred a complex media because organisms in the environment often encounter a complex nutritional source, and we felt that mimicking the condition of environment would best describe the antimicrobial and antibiofilm assays.

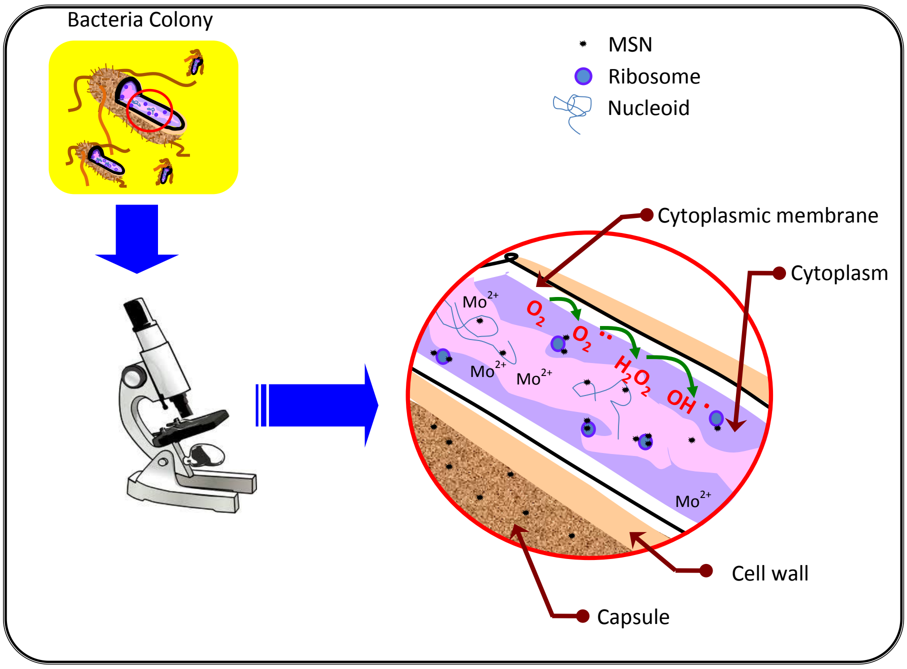

Figure 3.17 *Schematic depicting the possible mechanism of antimicrobial action by MSNs.*

A comparison of the reported antimicrobial activities of various nanomaterials against various microorganisms *vis-à-vis* the present work is shown in figure 3.18. However, in comparison to various reports on nanostructures of Ag, Pd, Fe-Pt, TiO_2, ZnO, MgO, CuO, etc, the MIC and MIB values in the present study are low [38, 55, 51, 56, 57, 58, 59, 60, 61, 62, 63]. Besides, they exhibit biofilm inhibition. Furthermore, a noble metal such as Ag, which is emerged as one of the best-studied nanoscale inorganic antimicrobial agent [56, 57] may have limited applications due to its higher cytotoxicity.

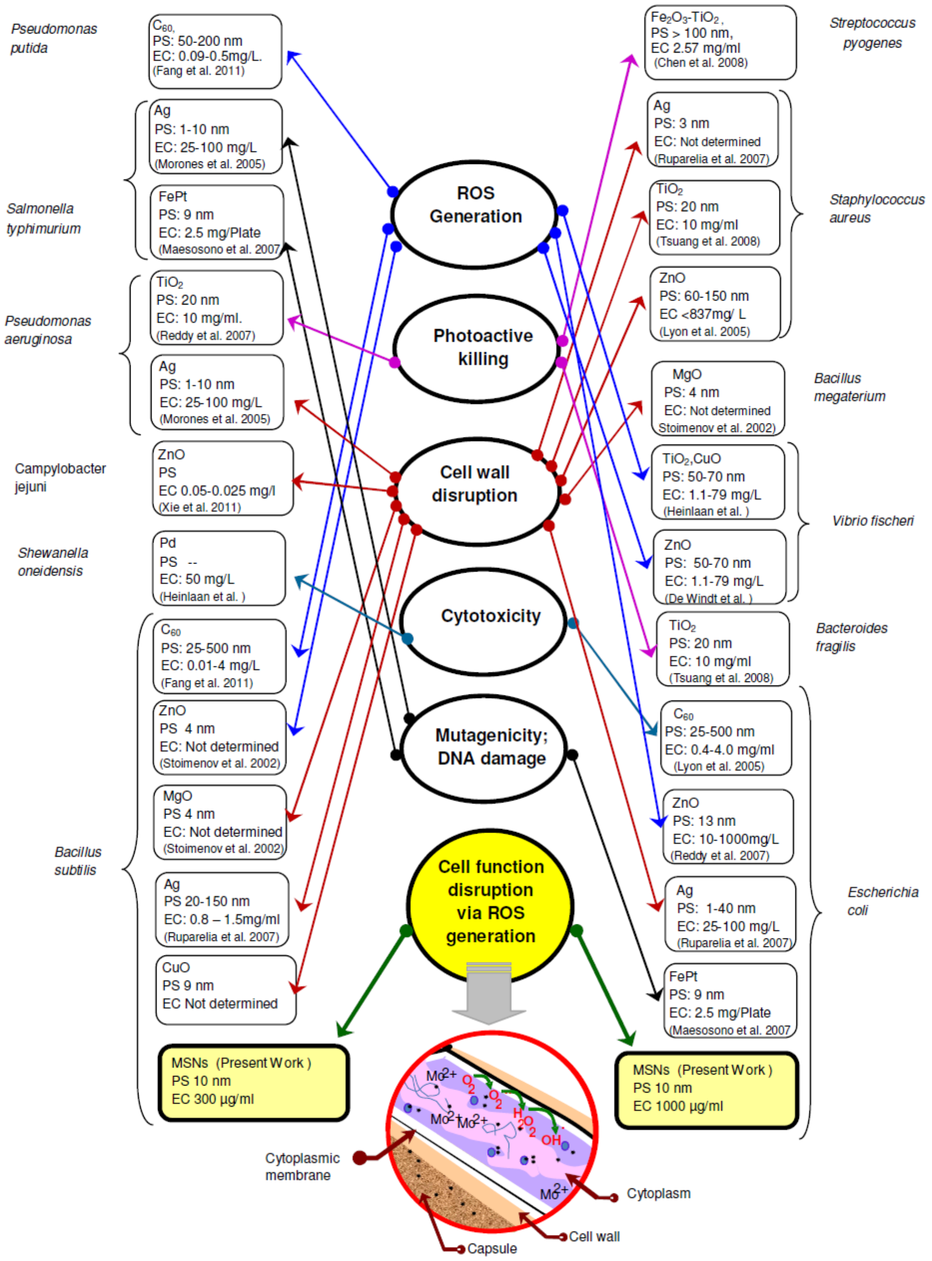

Figure 3.18 *Comparative illustration showing the antimicrobial effect of different inorganic nanoparticles and our MSNs on various gram-positive and gram-negative bacteria.*

Cytotoxicity Analysis:

The cytotoxicity studies of MSNs on Hela cell lines confirmed that MSNs are nontoxic (figure 3.19). When the cells of Hela were treated with MSNs particles and assayed for metabolic activeness as a measure of cell number, we found that the metabolic activity in MSNs treated cells were nearly the same as in control, indicating that they are nontoxic, and therefore can be deemed as biocompatible. Similarly, under a microscope, control cells were all adhered, uniform and confined to the monolayer, a typical of healthy cells, similar to MSNs treated cells, (black clusters are the aggregated MSNs on cells). Our cytotoxicity data correlates with a previous report on MSNs [64] as a biocompatible material making it a comprehensible choice as an antimicrobial agent.

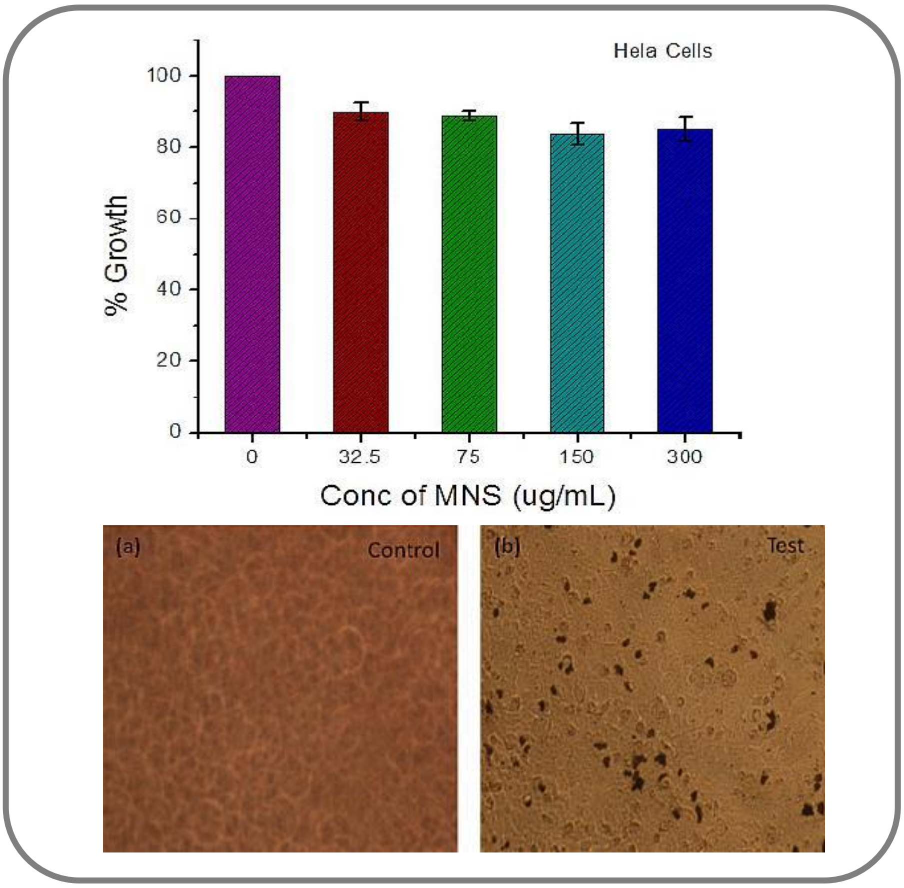

Figure 3.19 *The cytotoxicity study of the MSN against Hela cell. The MTT assay on Hela cells in the presence of MSNs particles shows a negligible decrease in percent growth, indicating non-cytotoxicity of MSNs (n = 3). Also, observation of Hela cells in the presence of MSNs particle shows uniformity of cells. The black spots in sample b are the aggregations of MSNs particles. a) Control cells and b) cells treated with MSNs*

3.3.4 Summary

Bacterial resistance to conventional medical antibiotics based on organic molecules is a serious concern for modern medicine. High prevalence of multidrug-resistant bacteria among bacteria-based infections decreases the effectiveness of current treatments and may culminate into contagion related deaths. In this context, nanoparticles tend to represent an effective solution for overcoming bacterial resistance. Precisely focusing on fringe benefits of inorganic chalcogenide nanoparticles, we accomplished hitherto unreported synthesis of biocompatible and non-cytotoxic molybdenum disulfide nanostructures at reduced reaction time using facile and ‘greener’ microwave assisted solvothermal route with the aim to study their antimicrobial attributes. The formulation containing MSNs demonstrated biofilm inhibition effect (detected using confocal microscopy and FESEM) which enhances the versatility of its applicability. Moreover, by quantitative determination of MIC and MBC, we established the prima-facie antibacterial property of our MSNs. We probed the possible mechanism of the antibacterial activity by detecting and measuring ROS, analyzing the change in enzymatic activity of redox enzymes (SOD and CAT) and also by observing the morphological images using fluorescence and electron microscopy. Interestingly, we could realize antimicrobial action by the disruption of cellular function as against rupture of the cell. Our studies and recent research on MSNs have shown that cytotoxicity is not a major concern for this class of nanoparticles which makes them a promising candidate for clinical trials in small animals. It is presumed that combining nanoparticles with antibiotics not only reduces the toxicity of both agents towards human cells by decreasing the requirement for high dosages but also enhances their bactericidal properties and such a hybrid approach can potentially overcome nanoparticle toxicity and offer a significant improvement in the design of antibacterial agents. Furthermore, combining antibiotics with nanoparticles may restore their ability to destroy bacteria that have acquired resistance to them. Therefore, such drug formulations based on MSNs may have vital and unprecedented applications in pharmaceutical and biomedical industry. Additionally, these formulations can be used for external applications and may be coated on medical devices/apparatus such as catheters and endoscopes to curtail the biofilm formation. Moreover, myriad applications of these nontoxic nanostructures may span areas such as hydrogen generation and storage, photo-catalysis, hybrid solar cells, drug storage and delivery.

References

[1] Semenov A. P. (2012) "On the possibility of improving antifriction properties of MoS_2 coatings by alloying" *Journal of Friction and Wear* 33(2):160–165.

[2] Kharisov B. I. (2008) "A review for synthesis of nanoflowers" Recent Patents on *Nanotechnology* 2: 190-200.

[3] Lauritsen J. V., Kibsgaard J, Helveg S, Topsøe H., Clausen B. S., Laegsgaard E. and Besenbacher F. (2007) "Size-dependent structure of MoS_2 nanocrystals" *Nature Nanotechnology* 53-58.

[4] Li Q., Walter E. C., Veer W. E., Murray B. J., Newberg J. T., Bohannan E. W., Switzer J. A., Hemminger J. C. and Penner R. M. (2005) "Molybdenum disulfide nanowires and nanoribbons by electrochemical/chemical synthesis" *J. Phys. Chem. B* 109:3169-3182.

[5] Huang X., Zeng Z., Bao S., Wang M., Qi X., Fan Z. and Zhang H. (2013) "Solution-phase epitaxial growth of noble metal nanostructures on dispersible single-layer molybdenum disulfide nanosheets" *Nature Comm.*1-8.

[6] Peng Y., Meng Z., Zhong C., Lu J., Yang Z. and Qian Y. (2002) "Tube- and ball-like amorphous MoS_2 prepared by a solvothermal method" *Mater. Chem. Phys.* 73:327–329.

[7] Berntsen N., Gutjahr T., Loeffler L., Gomm J. R., Seshadri R. and Tremel W. (2003) "A solvothermal route to high-surface-area nanostructured MoS_2" *Chem. Mater.* 15: 4498-4502.

[8] Wu H., Yang R., Song B., Han Q., Li J., Zhang Y., Fang Y., Tenne R. and Wang C. (2011)"Biocompatible inorganic fullerene-Like molybdenum disulfide nanoparticles produced by pulsed laser ablation in water" *ACS Nano.* 5 (2): 1276–1281.

[9] Li G., Jiang L., Pang S., Peng H. and Zhang Z. (2006) "Molybdenum trioxide nanostructures: the evolution from helical nanosheets to crosslike nanoflowers to nanobelts" *J. Phys. Chem. B* 110: 24472-24475.

[10] Li B. B., Qiao S. Z., Zheng X. R., Yang X. J., Cui Z. D., Zhu S. L., Li Z. Y. and Liang Y. Q. (2015) "Pd coated MoS_2 nanoflowers for highly efficient hydrogen evolution reaction under irradiation" *Journal of Power Sources* 284: 68–76.

[11] Xiong F., Cai Z., Qu L., Zhang P., Yuan Z., Kwadwo O., Asare, Xu W., Lin C. and Mai L. (2015) "Three-dimensional crumpled reduced graphene oxide/MoS_2 nanoflowers: a stable anode for lithium-ion batteries" *ACS Appl. Mater. Interfaces* 1-20.

[12] Huang K. J., Liu Y. J., Liu Y. M. and Wang L. L. (2014) "Molybdenum disulfide nanoflower-chitosan-Au nanoparticlescomposites based electrochemical sensing

platform for bisphenol a determination" *Journal of Hazardous Mater.* 276:207–215.

[13] Shinde M. D., Chavan P. G., Umarji G. G., Arbuj S. S., Rane S. B., More M. A., Joag D. S. and Amalnerkar D. P. (2012) "Field emission and photo-catalytic investigations on hierarchical nanostructures of copper doped CdS synthesized by 'kitchen-chemistry' approach" *J. Nanosci. Nanotech.* 12:3788-3798.

[14] Yang M. and He J. (2011) "Fine tuning of the morphology of copper oxide nanostructures and their application in ambient degradation of methylene blue" *J. Colloid Interface Sci*. 355 :15–22.

[15] Mogne T. L., Donner C., Martin J., Tonck A. and Millard-Pinard N. (1994) "Nature of super-lubricating MoS_2 physical vapor deposition coatings" *Journal of Vacuum Sci. Tech. A* 12 (4): 1998-2004.

[16] Beattie I. R. and Gilson T. R. (1969) "Oxide phonon spectra" *J. Chem. Soc. A* 2322-2327.

[17] Afanasiev P. (2008) "Synthetic approaches to the molybdenum sulfide materials" *Comptes Rendus Chimie* 11:159 - 182.

[18] Kam K. K. and Parkinson B. A. (1982) "Detailed photocurrent spectroscopy of the semiconducting group VIB transition metal dichalcogenides" *J. Phys. Chem*. 86 (4): 463–467.

[19] Yu H., Liu Y. and Stephanie L. B. (2008) "Synthesis of discrete and dispersible MoS_2 nanocrystals" *Inorg. Chem.* 47:1428-1434.

[20] Park J. C. and Song H. (2007) "Synthesis of polycrystalline Mo/MoO_x nanoflakes and their transformation to MoO_3 and MoS_2 nanoparticles" *Chem. Mater*. 19: 2706-2708.

[21] Jones S. A., Bowler P. G., Walker M. and Parsons D. (2004) "Controlling wound bioburden with a novel silver-containing hydrofiber dressing" *Wound Repair Regen* 12:288-94.

[22] Bjarnsholt T., Tolker-Nielsen T., Høiby N. and Givskov M. (2010) "Interference of *Pseudomonas aeruginosa* signalling and biofilm formation for infection control" *Expet. Rev. Mol. Med.* 12: e11.

[23] Weir E., Lawlor A., Whelan A. and Regan F. (2008) "The use of nanoparticles in anti-microbial materials and their characterization" *Analyst* 13:835–845.

[24] Shinde M., Patil R., Karmakar S., Bhoraskar S., Rane S., Gade W. and Amalnerkar D. (2012) "Antimicrobial properties of uncapped silver nanoparticles synthesized by DC arc thermal plasma technique" *J. Nanosci. Nanotech.* 12:887-893.

[25] Wu H., Yang R., Song B., Han Q., Li J., Zhang Y., Fang Y., Tenne R. and Wang C. (2011) “Biocompatible inorganic fullerene- like molybdenum disulfide nanoparticles produced by pulsed laser ablation in water” *ACS Nano* 5:1276–1281.

[26] Rapoport L., Fleischer N. and Tenne R. (2005) “Applications of WS_2 (MoS_2) inorganic nanotubes and fullerene-like nanoparticles for solid lubrication and for structural nanocomposites” *J. Mater. Chem.* 15:1782–1788.

[27] Chen J., Kuriyama N., Yuan H. T., Takeshita H. T. and Sakai T. (2001) “Electrochemical hydrogen storage in MoS_2 nanotubes” *J. Am. Chem. Soc.* 123:11813-11814.

[28] Imanishi N., Kanamura K. and Takehara Z. (1992) “Synthesis of MoS_2 thin film by chemical vapor deposition method and discharge characteristics as a cathode of the lithium secondary battery” *J. Electrochem. Soc.* 139:2082-2087.

[29] Thomalla M. and Tributsch H. (2006) “Photosensitization of nanostructured TiO_2 with WS_2 quantum sheets” *J. Phys. Chem. B* 110:12167-12171.

[30] Kopnov F., Leitus G., Yoffe A., Feldman I., Panich A. M. and Tenne R. (2006) “Electric transport properties and 1H NMR study of the fullerene-like WS_2 nanoparticles” *Phys. Stat. Sol.* 243: 3290-3296.

[31] Rapoport L., Fleischer N. and Tenne R. (2003) “Fullerene-like WS_2 nanoparticles: superior lubricants for harsh conditions” *Adv. Mater.* 15:651–655.

[32] Aharon E., Albo A., Kalina M. and Frey G. L. (2006) “Stable blue emission from a polyfluorene/layered-compound guest/host nanocomposite” *Adv. Func. Mater.* 16:980-986.

[33] Nemanič V., Žumer M., Zajec B., Pahor J., Remškar M., Mrzel A., Panjan P. and Mihailovič D. (2003) “Field-emission properties of molybdenum disulfide nanotubes” *Appl. Phys. Lett*. 82:4573–4575.

[34] Radisavljevic B., Radenovic A., Brivio J., Giacometti V. and Kis A. (2011) “Single-layer MoS_2 transistors” *Nature Nanotech.* 6:147-150.

[35] Li Q., Walter E. C., Veer W. E., Murray B. J., Newberg J. T., Bohannan E. W., Switzer J. A., Hemminger J. C. and Penner R. M. (2005) “Molybdenum disulfide nanowires and nanoribbons byelectrochemical/chemical synthesis” *J. Phys. Chem. B* 109:3169-3182.

[36] Afanasiev P., Geantet C., Thomazeau C. and Jouget B. (2000) “Molybdenum polysulfide hollow microtubules grown at room temperature from solution” *Chem. Commun.* 12:1001–1002.

[37] Afanasiev P. and Bezverkhy I. (2002) “Synthesis of MoS_x(5 > x > 6) amorphous sulfides and their use for preparation of MoS_2 monodispersed microspheres” *Chem. Mater*. 14:2826–2830.

[38] Peng Y., Meng Z., Zhong C., Lu J., Yang Z. and Qian Y. (2002) “Tube- and ball-like amorphous MoS_2 prepared by a solvothermal method” *Mater. Chem. Phys*. 73:327–329.

[39] Li W. J., Shi E. W., Ko J. M., Chen Z. Z., Ogino H. and Fukuda T. (2003) “Hydrothermal synthesis of MoS_2 nanowires” *J. Cryst. Growth* 250:418–22.

[40] Li Q., Li M., Chen Z. Q. and Li C. M. (2004) “Simple solution route to uniform MoS_2 particles with randomly stacked layers” *Mater. Res. Bull*. 39:981–986.

[41] Anon., National Committee for Clinical Laboratory Standards (NCCLS), Methods for dilution antimicrobial susceptibility tests for bacteria that grow aerobically, Approved standard, 5th ed. NCCLS document, M7-A5. (NCCLS, Wayne, PA, 2000).

[42] Liu S. B., Wei L., Hao L., Fang N., Chang M. W., Xu R., Yang Y. H. and Chen Y. (2009) “Sharper and faster “Nano Darts” kill more bacteria: a study of ntibacterial activity of individually dispersed pristine single-walled carbon nanotube” *ACS Nano* 3:3891–3902.

[43] Applerot G., Lellouche J., Perkas N., Nitzan Y., Gedanken A. and Banin E. (2012) “ZnO nanoparticle-coated surfaces inhibit bacterial biofilm formation and increase antibiotic susceptibility” *RSC Adv*. 2:2314-2321.

[44] Foucaud L., Wilson M. R., Brown D. M. and Stone V. (2007) “Measurement of reactive species production by nanoparticles prepared in biologically relevant media” *Toxicol Lett.* 174:1–9.

[45] Giannopolitis C. N. and Ries S. K. (1977) “Superoxide dismutases: I. occurrence in higher plants” *Plant Physiol.* 59: 309–314.

[46] Hetrick E. M., Shin J. H., Paul H. S. and Schoenfisch M. H. (2009) “Anti-biofilm efficacy of nitric oxide-releasing silica nanoparticles” *Biomaterials* 30: 2782–2789.

[47] Li G., Zhai J., Li D., Fang X., Jiang H., Dong Q. and Wang E. (2010) “One-pot synthesis of monodispersed ZnS nanospheres with high antibacterial activity” *J. Mater. Chem*. 20:9215–9219.

[48] Yamamoto O., Sawai J., Ishimura N., Kojima H. and Sasamoto T. (1999) “Change of antibacterial activity with oxidation of ZnS powder” *J. Ceram. Soc. Jpn.* 107: 853–856.

[49] Zhu X., Zhou J. and Cai Z. (2011) “The toxicity and oxidative stress of TiO_2 nanoparticles in marine abalone (Haliotisdiversicolor supertexta)” *Marine Pollution Bul.l* 63: 334–338.

[50] Zhang L., Jiang Y., Ding Y., Povey M. and York D. (2007) “Investigation into the antibacterial behaviour of suspensions of ZnO nanoparticles (ZnO nanofluids)” *J. Nanopart. Res.* 9: 479–489.

[51] Stoimenov P. K., Klinger R. L., Marchin G. L. and Klabunde K. J. (2002) “Metal oxide nanoparticles as bactericidal agents” *Langmuir* 18: 6679–6686.

[52] Dwyer D. J., Kohanski M. A. and Collins J. J. (2009) “Role of reactive oxygen species in antibiotic action and resistance” *Curr. Opin. Microbiol.* 12: 482–489.

[53] Nel A. E., Madler L., Velegol D., Xia T., Hoek E. M. V., Somasundaran P., Klaessig F., Castranova V. and Thompson M. (2009) “Understanding biophysico-chemical interactions at the nano–bio interface” *Nature Mater.* 8: 543-557.

[54] Su H. L., Chou C. C., Hung D. J., Lin S. H., Pao I. C., Lin J. H., Huang F. L., Dong R. X. and Lin J. J. (2009) “The disruption of bacterial membrane integrity through ROS generation induced by nanohybrids of silver and clay” *J. Biomater*. 30:5979–5987.

[55] Xie Y., He Y., Irwin P. L., Jin T. and Shi X. (2011) “Antibacterial activity and mechanism of action of zinc oxide nanoparticles against Campylobacter jejuni” *Appl. Environ. Microbiol.* 77:2325-31.

[56] Morones J. R., Elechiguerra J. L., Camacho A., Holt K., Kouri J. B., Ramírez J. T. and Yacaman M. J. (2005) “The bactericidal effect of silver nanoparticles” *Nanotech.* 16: 2346–2353.

[57] Ruparelia J. P., Chatterjee A. K., Duttagupta S. P. and Mukherji S. (2007) “Strain specificity in antimicrobial activity of silver and copper nanoparticles” *Acta. Biomater*. 4: 707–716.

[58] Maenosono S., Suzuki T. and Saita S. (2007) “Mutagenicity of water-soluble FePt nanoparticles in Ames test” *J. Toxicol. Sci*. 32: 575–579.

[59] Tsuang Y. H., Sun J. S., Huang Y. C., Lu C. H., Chang W. H. and Wang C. C. (2008) “Studies of photokilling of bacteria using titanium dioxide nanoparticles” *Artif. Organs*. 32: 167–174.

[60] Reddy K. M., Feris K., Bell J., Wingett D. G., Hanley C. and Punnoose A. (2007) “Selective toxicity of zinc oxide nanoparticles to prokaryotic and eukaryotic systems” *Appl. Phys. Lett.* 90: 213902-1–213902-3.

[61] Heinlaan M., Ivask A., Blinova I., Dubourguier H. C. and Kahru A. (2008) “Toxicity of nanosized and bulk ZnO, CuO and TiO_2 to bacteria *Vibrio fischer*i and *crustaceans Daphnia magna* and *Thamnocephalus platyurus*” *Chemosphere* 71: 1308–1316.

[62] De Windt W., Boon N., Van den Bulcke J., Rubberecht L., Prata F., Mast J., Hennebel T. and Verstraete W. (2006) “Biological control of the size and reactivity

of catalytic Pd(0) produced by Shewanella oneidensis" *Antonie Van Leeuwenhoek* 90:377–389.

[63] Lyon D. Y., Fortner J. D., Sayes C. M., Colvin V. L. and Hughe J. B. (2005) "Bacterial cell association and antimicrobial activity of a C_{60} water suspension" *Environ. Toxicol. Chem*. 24:2757–2762.

[64] Chen W. J., Tsai P. J. and Chen Y. C. (2008) "Functional Fe_3O_4/ TiO_2 core/shell magnetic nanoparticles as photokilling agents for pathogenic bacteria" *Small* 4:485-489.